https://doi.org/10.3311/PPci.44651
Creative Commons Attribution

Periodica Polytechnica Civil Engineering

Seismic Evaluation of the Experimentally Calibrated Multi-tiered Historical Masonry Structure

Amit Prajapati[1], Bin Zhao[1*], Anil Kasula[2], Satish Paudel[3]

[1] State Key Laboratory of Disaster Reduction in Civil Engineering, Tongji University, Shanghai, 200092, China
[2] Khwopa College of Engineering, Tribhuvan University, Bhaktapur, NP 44800, Nepal
[3] Department of Civil and Environmental Engineering, Princeton University, New Jersey, 08544, United States of America
[*] Corresponding author, e-mail: binzh@tongji.edu.cn

Received: 09 May 2026, 15 October 2026, Published online: 26 October 2026

Abstract

Historical structures in seismically active regions endure recurrent seismic events, posing significant challenges for their long-term preservation. Despite high seismic vulnerability, the dynamic properties of brick-mud mortar pagoda structures on soft soil remain largely unexplored through ambient vibration testing (AVT). This study presents a seismic evaluation of the Bhairabnath temple through an integrated AVT and nonlinear dynamic analysis framework. AVT identified fundamental frequencies of 1.58 Hz and 2.5 Hz in predominant directions, revealing inherent directional asymmetry. The identified frequencies were used to calibrate the finite element model through iterative updating, converging on the masonry material properties. Nine near-fault records with velocity pulses, spectrally matched to site-specific spectra, were applied in nonlinear time history analyses along both principal directions. Results revealed pronounced directional vulnerability, with the East-to-West (EW) direction exhibiting larger displacement demand and lower secant-to-elastic stiffness ratios than the North-to-South (NS) direction. The wide hysteresis loops and nearly twice the cumulative hysteretic energy dissipation in the EW direction indicate that it absorbed seismic demand primarily through inelastic damage rather than elastic resistance. Damage patterns confirmed tensile cracking as the dominant mechanism, concentrated mostly at the tapering upper section due to a disproportionate stiffness-to-mass ratio, at the fifth-floor openings caused by geometric stress concentration, and at the base corners due to cumulative overturning effects. These findings highlight the directionally asymmetric response of pagoda-style structures, providing a foundation for retrofitting strategies that prioritize direction-specific vulnerability alongside heritage conservation guidelines.

Keywords

ambient vibration test, historical masonry structure, nonlinear dynamic analysis, seismic assessment, pagoda-style

1 Introduction

Historical structures serve as physical embodiments of past civilizations, and their losses extend far beyond the economic values [1]. In seismically active regions, the frequent recurrence of earthquakes often threatens the structural integrity of the historical structures [2]. Without adequate technical expertise and rigorous maintenance procedures, the historical structures are at risk of vanishing [3]. A systematic seismic assessment is essential for the preservation of these historical structures [4]. For that, a non-destructive test paves the way for determining the dynamic characteristics of the existing structure, which is essential for the detailed seismic evaluation of the historical structure to comprehend the restoration, reconstruction, and retrofitting efforts.

Considering the construction period of the historical structure, knowledge regarding the material properties is often limited. Over time, the degradation of the material often results in a loss of material strength [5]. Further, acquiring precise material properties of existing structures is challenging and economically demanding, while in-situ tests are restricted or limited for historic structures [6, 7]. Conventional visual inspections often provide a superficial understanding of global structural behavior, failing to account for the internal complexities of such masonry structures. Moreover, non-destructive testing has become the standard approach for characterizing historical masonry without compromising material integrity, and a wide range of such techniques have been

Cite this article as: Prajapati, A., Zhao, B., Kasula, A., Paudel, S. " Seismic Evaluation of the Experimentally Calibrated Multi-tiered Historical Masonry Structure", Periodica Polytechnica Civil Engineering, 2026. https://doi.org/10.3311/PPci.44651

applied to heritage structures, including ambient vibration testing (AVT), ultrasonic pulse velocity, ground-penetrating radar, infrared thermography, and impact echo [8]. Despite their non-destructive nature, individual NDT techniques have inherent limitations when applied to historical masonry because of its heterogeneous, anisotropic, and composite nature [9]. These limitations highlight the need for complementary techniques capable of assessing the global structural response rather than only localized material characteristics.

Among such techniques, AVT is a widely adopted technique to determine the dynamic characteristics for condition assessment and model calibration [1, 10]. For the historical structures, ambient vibration serves as an indispensable tool for evaluating the global structural behavior [7]. It facilitates the identification of multi-mode responses and vital dynamic characteristics, including fundamental frequencies, mode shapes, and damping ratios. Generally, short-interval vibration records anticipate the structure's dynamic response and ensure structural health by detecting flaws that remain invisible [11, 12]. Gunaydin [13] evaluated the dynamic characteristics of the fire-exposed historical structure using the operational modal analysis technique for the reliability of the numerical model. Similarly, the dynamic behavior of the Chongwen Pagoda in China was measured through ground pulsation [14]. In Nepal, Jaishi et al. [15] conducted the ambient vibration test on the historical pagoda structure around the valley and proposed the relation for the natural period of the Nepalese historical structure. Later, Fujita et al. [16] updated the relation through a collective assessment of the microtremor test on different pagoda structures, along with some previously conducted tests. Moreover, field and laboratory tests conducted on the historical structures provide fundamental knowledge of their dynamic behavior. Such a test is essential given the inherent uncertainties in the material properties and construction methodologies, which are commonly not align with modern engineering standards. Despite these advantages, NDT results alone are insufficient for a holistic seismic evaluation. A robust numerical framework must be integrated with the experiment test result, allowing for a comprehensive seismic assessment that incorporates all structural components and their complex interactions.

The integrated framework between experimental NDT data and numerical modelling is best realized through Finite Element (FE) model updating. It transforms a numerical model to match the as-built state of the historical structure through calibration of initial stiffness and boundary conditions, hence capable of predicting damage patterns under various seismic scenarios [17]. Seismic assessment of historical structures relies on various computational approaches to achieve accurate numerical simulation [18, 19]. These approaches are essential for reducing structural vulnerability and identifying effective strengthening interventions against earthquakes. However, such an effort is further complicated by inherent uncertainties resulting from the unique construction procedure, undocumented past modifications, and undermining of original material properties. Notably, the aesthetically distinctive features of historical structures often introduce complex load transfer mechanisms, increasing their seismic vulnerability [20]. An effective way to deal with these uncertainties is through nonlinear dynamic analysis. This approach correctly depicts the dynamic response of the structure by adopting appropriate seismic intensity parameters. Therefore, a multi-scale seismic evaluation using varying seismic inputs is useful for the vulnerability assessment of historic structures [21].

Although brick and mud-mortar historic structures are widely used throughout the Kathmandu Valley, their dynamic behavior remains largely unexplored. Prior published data on the dynamic behavior of Nepalese pagoda-style temples remain limited, and the influence of the valley's deep, soft sedimentary soil layers on the seismic response of these structures has received even less attention. This study bridges this gap by investigating the dynamic properties of the Bhairabnath temple, a historic pagoda structure situated on the valley's soft soil, providing insight essential for its preservation. The field-derived properties obtained can further support the seismic assessment of other similar historical structures across the Kathmandu Valley, in place of generic, code-based assumptions.

This study experimentally identifies the dynamic response of the existing structure and highlights the seismic vulnerability of the historical multi-tiered Bhairabnath temple to quantify its seismic vulnerability. The experimental outcome calibrates the numerical model, which is then subjected to a nonlinear dynamic analysis performed in both directions. Further, the structural responses are evaluated in terms of displacement, drift ratio, acceleration, and damage states under a suite of near-field earthquakes matched to site-specific spectra. The findings provide critical insights into the seismic behavior of pagoda-type structures and ascertain evidence-based preservation and reinforcement strategies for future seismic events.

2 Physical description of the structure

The Bhairabnath temple is a seven-story building made of brick, earth, mortar, and wood. It features a typical pagoda-style building with its distinctive multi-tiered construction. The structure has three overhanging roofs located on the third, fifth, and seventh floors, as presented in Fig. 1. Unlike other tiered structures that typically adopt a square plan, this temple possesses a unique rectangular base. The Bhairabnath temple, located in Bhaktapur Durbar Square, Nepal, is a typical example of a pagoda-style multi-tiered architecture with wide overhanging roofs. Following its complete collapse during the 1934 Nepal-Bihar earthquake (Mw 8.2), the existing structure was entirely rebuilt [22]. Subsequently, it suffered major structural damage during the 1988 Udyapur (Mw 6.6) and 2015 Gorkha earthquake (Mw 7.6), as presented in Fig. 1.

The primary load-bearing components of the structure are the external walls, which extend vertically in three distinct sections as shown in Fig. 1. At each roof level, the external walls of the upper floor are set back inward by a certain distance, resulting in an irregular vertical configuration. The inner walls rest on horizontal timber floors, contributing to a complex structural load transfer mechanism. The tiered roof of the Bhairabnath temple comprises a complex framework of beams, struts, and rafters working in conjunction with the exterior walls. Due to the reduction in exterior wall dimensions at each tier, three box-type exterior wall sections are formed. Accordingly, the structure is categorized into Bottom (B), Middle (M), and Top (T) sections. The external dimensions are 12.60 × 7.70 m (B), 9.80 × 4.84 m (M), and 7.34 × 2.34 m (T), with corresponding wall thicknesses of 0.93 m, 0.75 m, and 0.65 m, respectively, as shown in Fig. 1. The thicker walls at the lower floors compared to the upper floors represent a typical feature of masonry construction.

The structure incorporates a central wall extending from the foundation to the sixth floor. The thickness of the central wall varies depending on the box section of the structure, measuring 0.93 m and 0.60 m at the bottom and middle sections, respectively. Notably, the central wall is not connected properly to the side walls, showing discontinuities at the second, third, and fifth floors.

As the setback configuration reduces the external wall, those box sections rest on the timber joists on the third and fifth floors that extend horizontally, connecting the long external walls. In the structural framework, these joists are essential for sustaining the entire structural load above them. Additionally, they serve as flexible floor components that are fastened to the exterior using timber pegs. The Bhairabnath temple highlights the complex construction techniques employed in traditional Nepalese pagoda architecture, particularly the structural integration of the masonry sections.

3 Methodology

The study systematically outlines the experimental procedure and nonlinear dynamic analysis performed on the multi-tiered Bhairabnath Temple. Initially, A comprehensive literature review of historical records and documentation on the temple and similar heritage structures established the research framework. With permission and collaboration from the local authority, structural measured drawings and on-site non-destructive measurements were collected. Subsequently, the dynamic characteristics

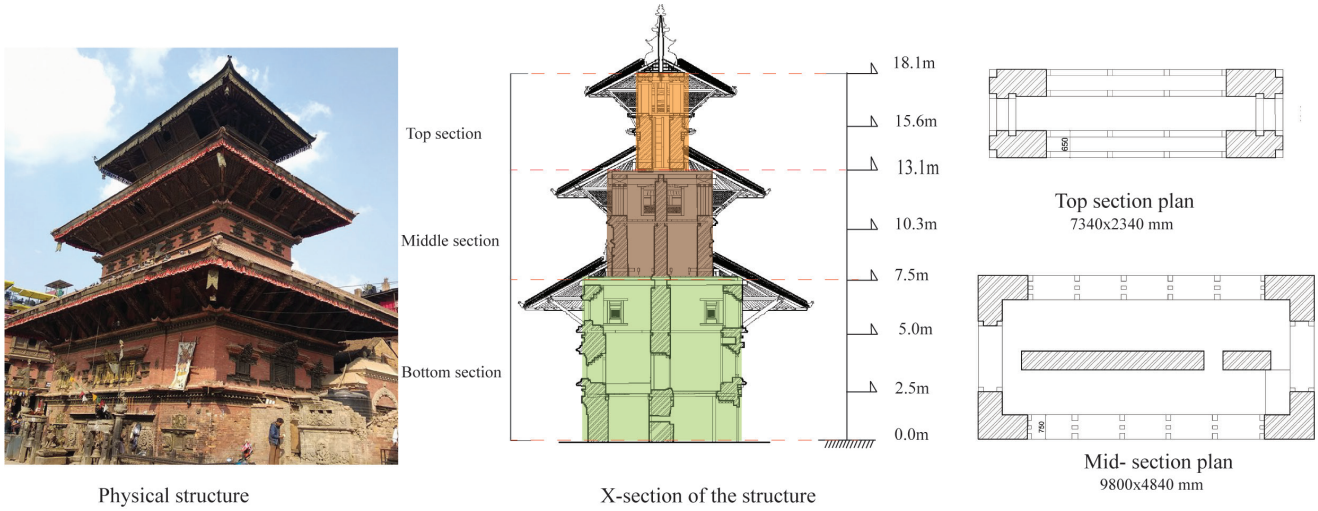


Fig. 1 Physical description of the Bhairabnath temple

of the structure were determined using the experimental test results. Later, a detailed finite element model was developed and calibrated using in-situ test outcomes. The research methodology integrates experimental and numerical approaches and performs non-linear dynamic analysis.

3.1 Ambient vibration test

In the existing historical structure, a non-destructive ambient vibration test is the most reliable in-situ test for the identification of dynamic characteristics, which captures low-frequency vibration of the structure. Such testing is widely preferred for historical structures to assess the dynamic behavior because it is non-destructive and easy to implement, making it particularly suitable for highly sensitive and vulnerable structures [17]. A three (X, Y, Z) component velocity sensor, McSEIS-AT, manufactured by OYO Corporation, deployed at the center of the floors, measures the ambient vibration of the structure. Three sensors were positioned near the centroid of the top floor of each section, and one sensor measured free-field vibration. All the sensors measured low-frequency vibration simultaneously using built-in GPS at the ground, third, fifth, and seventh floors of the structure, as shown in Fig. 2. The simultaneous recording enabled the identification of the dynamic parameters of the structure, such as predominant frequency, mode shapes, and damping ratio. The raw data were recorded at a sampling frequency of 250 Hz, which was kept undisturbed for 15 min.

Fig. 2(a), 2(b), and 2(c) illustrate the velocity power spectral density (PSD) derived from ambient vibration testing (AVT) across the EW-, NS-, and V-directions. The spectral plots highlight distinct, well-defined peaks, which correspond to the structure's predominant natural frequencies under stochastic excitation such as wind and microtremors. The horizontal (EW and NS) spectra effectively characterize the lateral translational modes, and the vertical (V) spectra provide insight into vertical components. In the EW spectra, three distinct frequency peaks are observed at 1.59, 3.15, and 4.75 Hz, while the NS spectra have one distinct frequency peak at 2.50 Hz. The significant difference in the frequency in EW and NS spectra is due to the variation in stiffness caused by directional variability of the structure.

Further, Operational Modal Analysis (OMA) was applied as a tool to extract the modal parameters such as natural frequencies and mode shapes from the experimental vibration results [23]. OMA is performed using the enhanced frequency domain decomposition technique for the determination of the dynamic characteristics. The modal parameters are determined through peak picking in the singular value decomposition generated from the spectral density response [5]. These identified modal parameters provide a foundation for the subsequent calibration of the Finite Element (FE) model.

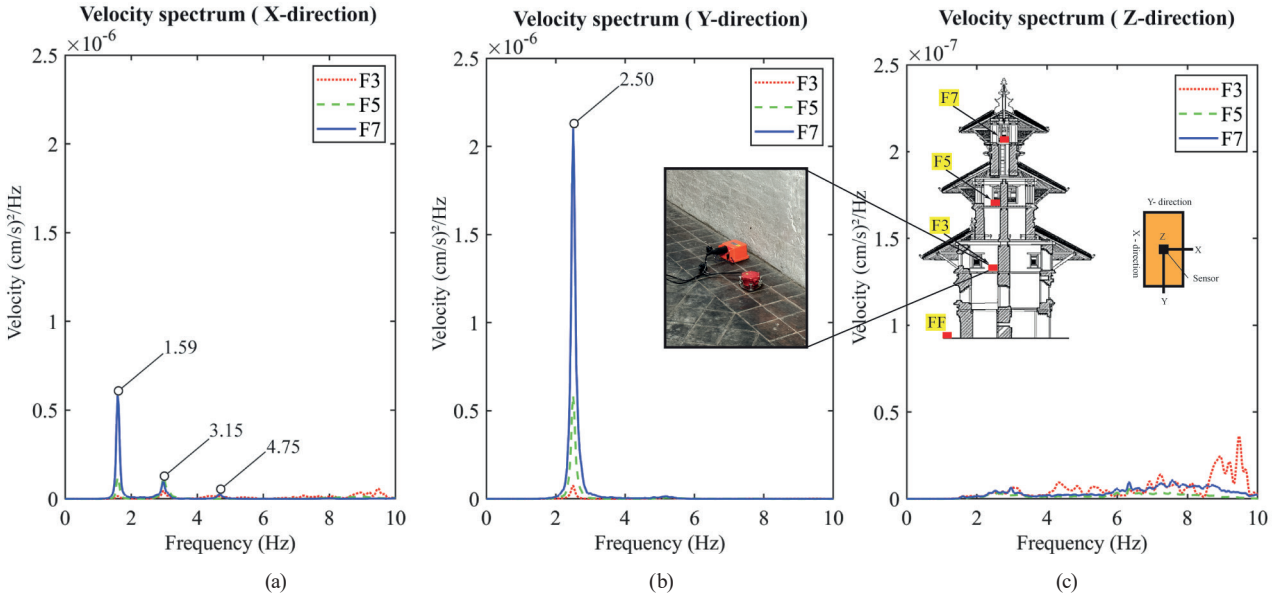


Fig. 2 Velocity power spectrum plot from ambient vibration test (a) EW- direction, (b) NS- direction, and (c) V- direction along with the sensor locations and orientation

3.2 Numerical modelling

Historical structures are structurally complex and involve inherent uncertainties, which require advanced computational frameworks for reliable seismic assessment. The finite element method is employed to explicitly model major structural components and systematically integrate structural irregularities. Nonlinear dynamic analysis of the Bhairabnath temple was conducted using the sophisticated finite element-based Abaqus [24]. The simulation utilizes an implicit time integration solution technique to ensure numerical stability and effectively capture the transient structural response. Robust convergence of the numerical solution was reliably achieved by applying the iterative Newton-Raphson method at each time increment. This rigorous methodology facilitates the precise monitoring of energy dissipation and damage evolution within the complex structure.

Initially, the numerical model was developed by discretizing the structure into individual structural components. To facilitate computational efficiency with low demand, a macro modelling approach was adopted to achieve the research objective [25]. Eight-node linear brick elements with reduced integration (C3D8R) were assigned to the major structural masonry walls and timber beams. The use of the C3D8R elements is a reliable way to capture the flexural and shear response of the thick masonry walls [26]. Similarly, two-node beam elements (B31) were assigned for architectural components, including the roof truss, windows, and doors. The resulting global model comprised 119966 elements and 236915 nodes. The mesh sensitivity analysis yielded a mesh size of 300 mm for masonry walls and a 100 mm mesh for timber elements to ensure a high level of accuracy, maintaining numerical efficiency. The major load-bearing masonry and the supporting timber framework are the major structural components, as shown in Fig. 3. This modeling approach accurately represents the structure's load-bearing mechanisms and structural interactions, providing a robust framework for dynamic analysis.

The structure is modelled in three different sections. The bottom section is wider in dimension than the consecutive upper section. For each section, the exterior wall-to-wall connections are modelled with kinematic constraints tied to simulate realistic structural behavior. Tie constraints allowed the formation of vertical cracks between connected walls, particularly during out-of-plane mechanisms. Further, a continuum model simulates a perfectly connected system where all the elements behave as an integrated structure [23]. However, in unreinforced masonry structures, wall-to-wall connections are typically formed through a toothing mechanism, which can be explicitly captured in micro-modelling [27, 28]. Despite this limitation, macro modelling provides an efficient approach to global structural analysis while maintaining computational feasibility. However, the central wall is not connected to the external wall, that represent some discontinuities in the connection. On the second, third, and fifth floors, the central wall is not connected to either side of the external wall, as shown in Fig. 4.

All the floors are represented with solid timber elements, and the layout of the structure is represented in Fig. 3. Timber beams on the third, fifth, and seventh floors were tied using kinematic tie constraints with external masonry walls. Additionally, a base plate is inserted at the base of each wall section to support the upper masonry walls, ensuring proper load distribution. Moreover, the

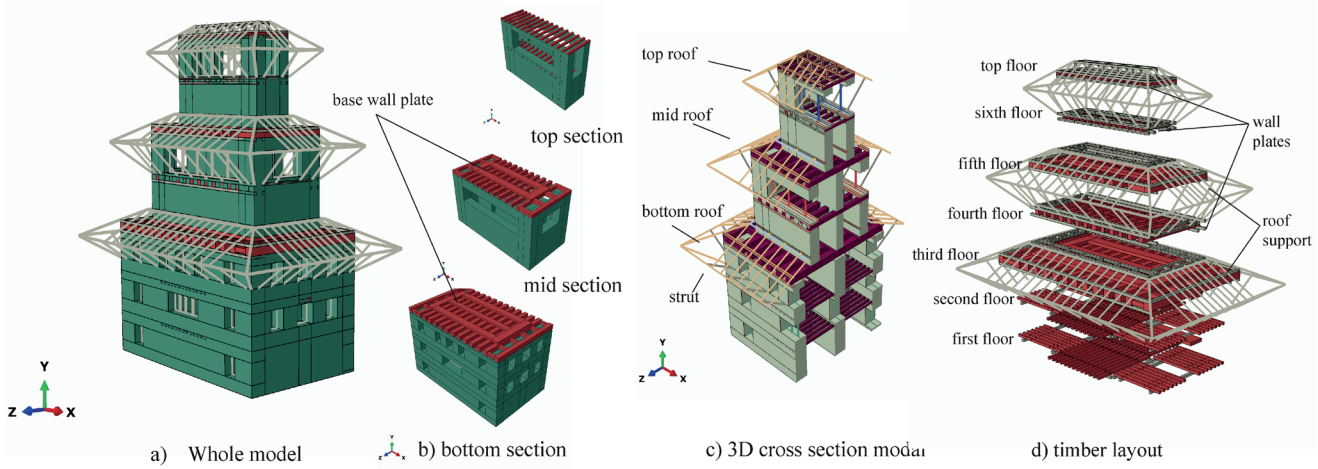
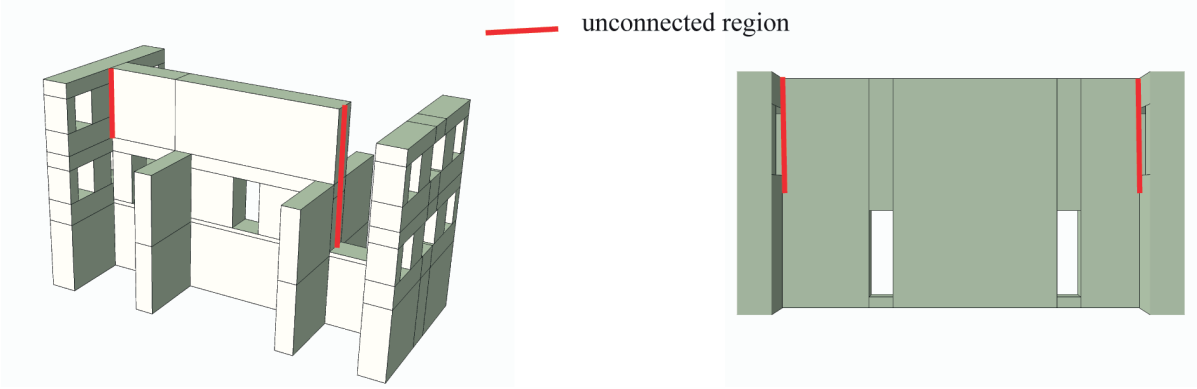


Fig. 3 Detail representation of the structural components in modelling (a) Whole model, (b) Bottom section, (c) 3D cross section modal, (d) Timber layout



(a) (b)

Fig. 4 Unconnected region between external wall and central wall (a) Bottom section and (b) Middle section of the structure

beams are embedded in the walls on the intermediate floor. The three-dimensional solid-in-solid embedded constraint was adopted, where the masonry walls were assigned as host elements and timber elements as embedded elements. This constraint ensures that the degree of freedom of nodes in the embedded timber elements is tied to the corresponding degree of freedom of the host elements. Both the nodes are effectively coupled during motion, which resembles the structure representing a semi-flexible floor. The roofs were modelled with two nodal beam elements (B31) and assigned MPC constraints.

3.3 Material modelling

Understanding material properties in the existing masonry structure is challenging due to inherent uncertainties and constraints [23, 29]. Undoubtedly, the mechanical properties are influenced by multiple factors, including the mineralogical composition of its constituents, which varies based on the source of extraction [30]. The mixing and laying process also introduces non-homogeneity, making masonry anisotropic [3]. Generally, masonry structures adopt three different modelling strategies: micro-modelling, simplified modelling, and macro-modelling [4]. In micro-modelling, units and mortar joints are modeled separately with their own constitutive laws and interface behavior, whereas simplified micro-modelling uses expanded units where joints are lumped into zero-thickness interface elements. This study adopted the macro-modelling technique for masonry structures, where the equivalent isotropic continuum idealization represents the average mechanical response of the unit-mortar assemblage. It is an accepted approach for seismic assessment of geometrically complex historical structures, as it allows the simulation of full-scale elements while still capturing localized damage. The mechanical properties of mud mortar brick masonry remain comparatively under-investigated in the literature. Nonetheless, a few studies have specifically addressed the mechanical characterization of this masonry type, which is presented in Table 1. For this study, the essential brick-mud masonry properties were adopted from the uniaxial compression and tension experiments performed on a series of brick masonry specimens [30]. Moreover, the initial material properties require calibration to be used in the numerical simulation to resemble the actual dynamic properties. The calibrated material properties of the structure in the numerical model are presented in Table 2 [31–33].

Table 1 Mechanical properties for the historical mud mortar masonry structure

Type	Material properties			Ref.
	E (MPa)	Poisson ratio (η)	Density (kg/m³)	
Brick mud masonry	150		1800	[20]
Brick mud masonry	400		1800	
Sal wood	12500		800	
Brick masonry	280–485	0.25	1800–2000	[31]
Timber	12500	0.12	900	
Brick masonry	160		1800	[32]
Timber	10000		900	
Brick Masonry	274	0.21	1800	[33]
Timber	12500	0.3	800	

Table 2 Elastic material properties of masonry wall and timber

Material	E (MPa)	γ (kg/m3)	η	f_c (MPa)	f_t (MPa)	Ref.
Mud mortar-brick masonry						
Initial	180	1630	0.25	1	0.045	[30]
Calibrated	150	1800				
Timber	12500	800	0.2	-	-	[20]

E = Young's modulus , γ = Density, η= Poisson's ratio, f_c = compressive strength and f_t = tensile strength

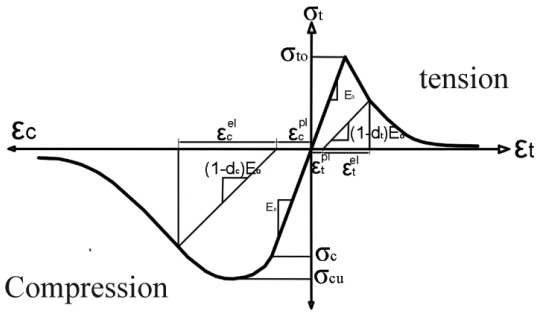


Fig. 5 Elastic and inelastic properties of brick masonry having mud mortar in compression and tension zone

The widely used Concrete Damage Plasticity (CDP) model accounts for the material inelastic-plastic behavior [34]. The CDP model was developed for monotonic loading for concrete analysis [35], which was later modified [36] to accommodate cyclic and dynamic loading. However, its application in masonry structure analysis has yielded good results [37]. The failure mechanism for the continuum-based damage plasticity model assumes tension cracking and compression crushing. The plastic zone develops beyond the yield limit, which is characterized by strain softening and stress hardening in compression. It allows the model to simulate the progressive degradation of masonry under different loading conditions. The adopted brick-mud masonry properties under elastic and inelastic behavior under compression and tension are shown in Fig. 5.

The constitutive plasticity flow model for the nonlinear analysis accounts for elastic and plastic stiffness degradation [35]. It uses isotropic damaged elasticity combined with no associated multi-hardening plasticity to represent the irreversible damage that occurs during fracturing. The damage criteria initiate the degradation of stiffness, commonly called compression and tension damage. When damage is triggered, the scalar damage variable reduces the elastic modulus (E) under uniaxial conditions, as shown in Eq. (1).

$$E = \left(1-d\right)E_0 \tag{1}$$

where, d is the damage reduction variable, and E_0 is the undamaged elastic modulus

Based on the theory of Plasticity, the strain tensor ε decomposes into elastic ε^{el} and plastic part ε^{pl} The damage occurs only in the softening zone, representing the stiffness reduction. The stress-strain relations under uniaxial tension and compression are represented by Eq. (2).

$$\sigma_t = \left(1-d_t\right)E_0\left(\varepsilon_t - \varepsilon_t^{pl}\right) \tag{2}$$

where, d^t and d^c represent scalar damage variables in tension and compression, ranging from 0 to 1.

For the CDP yield function, under compression and tension, the strength evolution was developed by [36], as shown in Eq. (3).

$$F\left(\bar{\sigma},\tilde{\varepsilon}^{pl}\right) = \frac{1}{1-\alpha}\left(\bar{q} - 3\alpha\,\bar{p} + \beta\left(\tilde{\varepsilon}^{pl}\right)\langle\hat{\bar{\sigma}}_{max}\rangle - \gamma\langle-\hat{\bar{\sigma}}_{max}\rangle\right)$$
$$-\hat{\bar{\sigma}}_c\left(\tilde{\varepsilon}_c^{pl}\right) = 0 \tag{3}$$

Where

$\bar{p}$ is the effective hydrostatic pressure,

$\bar{q}$ is the Von Mises equivalent of effective stress,

$\hat{\bar{\sigma}}_{max}$ Maximum principal stress,

σ_{b0}/σ_{c0} ratio of equiaxial compressive yield stress to uniaxial compressive yield stress,

K_c ratio of second stress invariant,

$\overline{\sigma_c}\left(\tilde{\varepsilon}_c^{pl}\right)$ and $\bar{\sigma}_t\left(\tilde{\varepsilon}_t^{pl}\right)$ Effective compressive and tensile cohesion stress,

α is the ratio between the initial equi-biaxial and uniaxial compressive yield stresses σ_{b0}/σ_{c0} (Eq. (4)).

$$\alpha = \frac{\left(\sigma_{b0}/\sigma_{c0}\right)-1}{2\left(\sigma_{b0}/\sigma_{c0}\right)-1}; 0. \le \alpha \le 0.5 \tag{4}$$

$\beta\left(\tilde{\varepsilon}^{pl}\right)$ is a function of the effective cohesion stresses, (Eq. (5)).

$$\beta\left(\tilde{\varepsilon}^{pl}\right) = \frac{\overline{\sigma_c}\left(\tilde{\varepsilon}_c^{pl}\right)}{\bar{\sigma}_t\left(\tilde{\varepsilon}_t^{pl}\right)}\left(1-\alpha\right) - \left(1+\alpha\right) \tag{5}$$

K_c is the ratio of the second stress invariant on the tensile meridian q(TM) to that on the compressive meridian q(CM), at the same hydrostatic pressure p, evaluated at initial yield (Eq. (6)).

$$K_c = \frac{q\left(TM\right)}{q\left(CM\right)} 0.5 \le K_c \le 1.0 \tag{6}$$

γ is a function of K_c (Eq. (7)).

$$\gamma = \frac{3\left(1-K_c\right)}{2K_c - 1} \tag{7}$$

In homogeneous continuum masonry, the plastic parameters, such as dilation angle and viscosity parameter, significantly influence the post-elastic response of masonry. However, variations in the elastic yield surface due to changes in the dilation angle do not affect the elastic yield surface, while increased viscosity parameters induce fictitious overstrength due to high dilatancy. This study follows the calibrated macro-model range of

Rainone et al. [37] for a dilation angle (ψ = 35°) and an optimized viscosity parameter (μ = 0.0001) in the CDP model, selected to limit artificial overstrength while maintaining numerical stability. Other parameters like eccentricity(e), σ_{b0}/σ_{c0} (ratio of initial equi-biaxial to initial uniaxial compressive yield stress), and K (the ratio of the second stress invariant) on the tensile meridian were set to 0.1, 1.16, 0.667, and 0.0001, respectively [24, 37].

3.4 Selection of time history data

For the nonlinear dynamic analysis, the selection of ground motion data is crucial, particularly for the historical structure. Due to the inherent low mechanical strength and limited ductility, historical structures are acutely sensitive to cumulative energy dissipation, which facilitates progressive structural degradation and stiffness loss. However, the dominating pulse nature of near-fault motion generates substantial energy within a short duration, producing high instantaneous seismic demand on the structure [38]. Numerous studies have demonstrated that the earthquake having velocity pulses, typically near-fault earthquakes, produces severely damage to structures [39, 40]. Bilgin [41] investigated the masonry structure using near- and far- fault earthquakes and demonstrated that near-fault earthquakes exert greater damage to the masonry structure than the far-fault earthquakes. In this study, nine earthquakes with distinct pulses in the seismic waveform are selected from the PEER database [42], which are presented in Table 3, following the guidelines of ASCE/SEI (7-10) [43]. The nine near-fault ground motion records used in the nonlinear dynamic analysis were selected considering Rupture distance (Rrup) less than 15 km and Moment magnitude (Mw) ranging from 5 to 8. Additionally, a different range of fault mechanisms, such as strike-slip (Ss), normal fault (N), reverse fault (R), and reverse oblique fault (Ro), are considered in order to represent the variability expected in near-fault ground motion characteristics. All selected records correspond to stations on bedrock, defined here as sites with a time-averaged shear-wave velocity over the upper 30 m (Vs30) greater than 700 m/s. The selected ground motions were matched with the target spectra generated by Prajapati and Zhao [44] for the site, as shown in Fig. 6.

Table 3 Selected ground motions for the nonlinear dynamic analysis

Sn	Earthquake	Year	Mw	Fault	Rrup (km)	PGA (g)
1	Coyote	1979	5.74	Ss	3.11	0.42
2	Irpnia	1980	6.9	N	8.18	0.19
3	Morgan Hill	1984	6.19	N	9.87	0.29
4	Northridge	1994	6.69	R	5.92	0.43
5	Koceli_1161	1999	7.51	Ss	10.92	0.26
6	Koceli_1165	1999	7.51	SS	7.21	0.23
7	ChiChi	1999	7.62	Ro	2.74	0.34
8	Laquila	2009	6.3	N	5.38	0.36
9	Duzce	1999	7.14	Ss	2.65	0.30

Spectral matching to the target design spectrum was performed in SeismoMatch using a two-step adjustment procedure [45]. The first step is to match the spectrum over the 0.05 to 2 s period range to align the selected earthquake spectra with the target spectra, followed by a refinement pass extending the matching period up to 4 s to reduce local residual misfit while preserving the non-stationary amplitude, phase, and near-fault pulse characteristics of the original records. Goodness-of-fit was quantified via mean square error over the matching period range, with records accepted if less than 0.3. Fig. 6 shows the resulting spectral compatibility of the nine matched records with the target spectrum.

4 Experimental results and FEM calibration

The experimental test setup on the Bhairabnath temple was described in Section 3.1. With the limited instruments installed, the dynamic characteristics of the structure were identified through OMA techniques. OMA is a widely used tool to determine the modal frequencies and shapes from the experimental vibration data. All the AVT sensors were installed at the geometric center of the plan at the ground floor and at three instrumented levels, recording translational accelerations in the two horizontal orthogonal directions (EW and NS) and the vertical direction. Table 4 shows the experimentally identified frequencies of the structure.

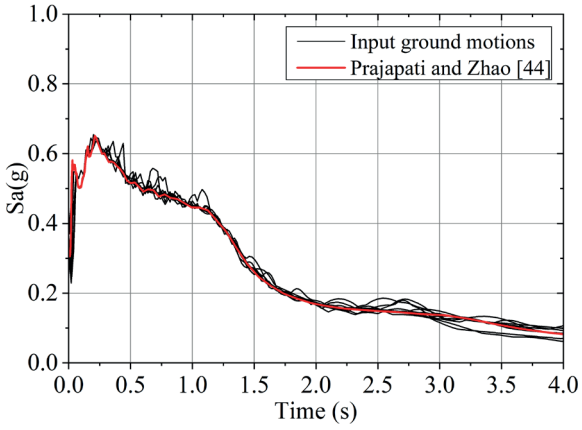


Fig. 6 Spectral acceleration of each earthquake matched with the target spectra

The numerical model accounts for different uncertainties, which are subject to the interaction between the walls and the timber joints, the mechanical properties of the wall, and timber. However, a perfect model cannot be expected for the historical structure. This work is done for the minimization of the uncertainties to ensure the reliability of the model. The uncertinities remains on the geometric dimensions are therefore adjusted through the field survey. Moreover, the difficulty in adopting the material properties of the existing masonry structure is minimized using the AVT on the structure. The test ascertains the global behavior of the structure rather than local behavior.

The elastic modulus of the brick mud mortar masonry was determined through an iterative finite element model updating procedure using the AVT. The calibrated mechanical properties are tabulated in Table 4. Initially, the elastic modulus of the structure was adopted from the wall-based experimental test result conducted by Endo et al. [30]. Then, the elastic modulus was incrementally adjusted, and the frequency modal analysis was performed until the numerically computed natural frequencies converged with the corresponding AVT-derived experimental frequencies, with a frequency discrepancy of less than 5%. Later, the calibrated mode shapes were also matched with the MAC value for further confirmation. The resulting calibrated properties, elastic modulus (E = 150 MPa) with an associated density (ρ = 1800 kg/m³), were subsequently verified against published material properties for brick mud mortar masonry in comparable Nepalese historical structures, presented in Table 1. It falls within the reported range of 150–800 MPa for a masonry configuration of similar construction and mortar composition. This confirms that the calibrated value is not only numerically convergent but also physically representative of the material class under study. The discrepancies may involve homogenization of material, generalized dimensions, connection constraints, and other unknown factors. The calibration ensures the replication of the actual dynamic behavior of the structure in numerical form.

Table 4 Comparison of calibrated frequency with experimentally obtained frequency and mass participation ratio of numerical modal at different modes

Mode	1	2	3	4	5	6
AVT frequency (Hz)	1.59	2.50	-	3.15	4.75	6.00
Calibrated numerical (Hz)	1.58	2.39	3.25	3.29	4.86	6.22
Error (%)	0.63	4.43	-	4.44	2.33	3.66
Ratio of effective mass to total mass						
EW - direction (%)	58.09	0.00	0.25	23.94	0.00	0.00
NS - direction (%)	0.00	71.23	0.00	0.00	28.69	0.00
V - direction (%)	0.000	0.00	0.00	0.00	0.00	99.86

As the numerical model computes all vibration modes of the full three-dimensional structure, some modes identified numerically could not be recovered experimentally. In the case of Mode 3, as reported in Table 4, there is no calibrated experimental frequency. This mode distribution is consistent with a torsion dominated by rotation about the vertical axis rather than translation. The effective modal mass participation ratios computed numerically show that Mode 3 mobilizes only 0.25% of the mass in the EW direction and 0.00% in both the NS and vertical directions. Since the AVT sensors were positioned at the plan centroid, where the translational response to a purely torsional mode is theoretically minimal, this mode could not be excited to a measurable level and was therefore not detected in the ambient vibration records. Consequently, the modal calibration was based on the modes exhibiting significant effective mass participation in the principal directions. These govern the global dynamic response measured experimentally. Hence, Mode 3 was excluded from the calibration criteria given its negligible contribution to the global translational and vertical response, however, the calibrated frequency of 3.25 Hz is reported in Table 4 for completeness rather than as a calibration target.

Operational modal analysis was used to determine the mode shapes of the existing structure, with each mode normalized to unity to obtain the corresponding mode shape vectors. The results indicate that the first two modes correspond to translation in the EW and NS directions, respectively, while the fourth and fifth modes represent higher-order bending in the EW and NS directions, respectively. The mode sixth is vertical translation mode, as shown in Table 4, which has the highest effective mass ratio in the vertical direction. Fig. 7 compares the frequencies and mode shapes from the numerical model with those from the experimental ambient vibration testing (AVT). The first mode exhibits excellent agreement, while the remaining modes show acceptable deviations within 5%. Furthermore, the close alignment between the AVT results and the calibrated finite element model confirms the adequacy of the adjusted material parameters and the overall reliability of the numerical model for the accurate representation of the dynamic behavior of the structure.

Further, the mode shape correlation was validated using the Modal Assurance Criterion (MAC) to quantify the agreement between the experimentally and numerically

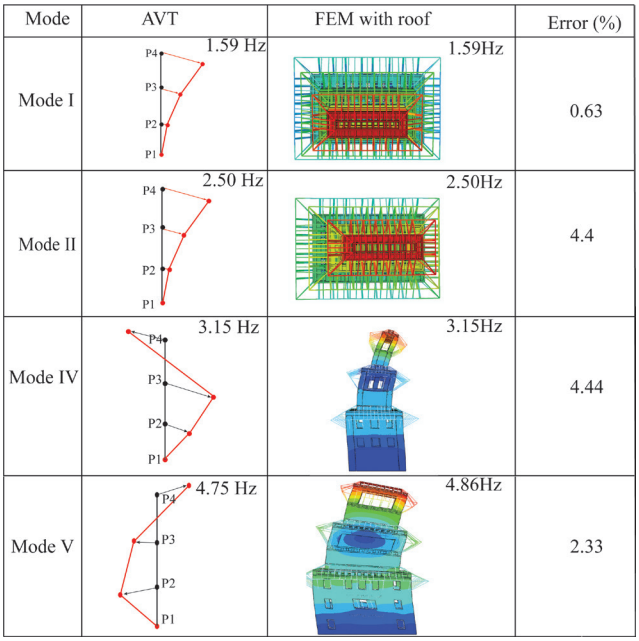


Fig. 7 Comparison of experimentally identified mode shapes and numerically obtained mode shapes.

obtained mode shapes. MAC was computed using the mode shape ordinates at the three instrumented floor locations, with numerical mode shapes extracted at nodes coincident with the physical sensor positions. Both numerical and experimental shapes are normalized to unit amplitude at the reference DOF before comparison. The complete MAC matrix for the five experimentally identifiable modes is presented in Table 5. The diagonal terms range from 0.786 to 0.996, indicating overall mode shape correlation, though not uniformly excellent across all modes. Modes 1, 2, and 6, which mobilize the dominant share of the structure's effective mass in a principal direction, as presented in Table 5. High diagonal MAC values show the strongest correlation, confirming that the modes governing the global dynamic response are well represented by the calibrated model. However, Mode 4 shows a comparatively lower MAC value of 0.786, the weakest among the retained modes. This is attributed to its low effective mass participation around 22.48% in the EW direction. The corresponding off-diagonal MAC between numerical Mode 4 and experimental Mode 5 indicates that, when reduced to the three available measurement DOFs, these two modes exhibit similar translational amplitude distributions, consistent with the coupling between closely spaced modes. This result should therefore be interpreted as acceptable rather than excellent agreement for Mode 4, reflecting both the physical mode behavior of the structure and the limited spatial resolution of the three-point sensor array, rather than a modeling deficiency. Overall, the MAC results support the calibration procedure adopted, while highlighting that correlation confidence should be weighted by each mode's effective mass contribution rather than treated uniformly across all modes.

Table 5 MAC values of experimental and numerically identified mode shapes

Num \ Exp	1	2	4	5	6
1	0.996	0.9996	0.002	0.147	0.624
2	0.983	0.992	0.001	0.101	0.648
4	0.278	0.237	0.786	0.781	0.040
5	0.291	0.253	0.710	0.983	0.035
6	0.576	0.645	0.027	0.030	0.958

5 Nonlinear dynamic performance assessments

For the existing historical masonry structure, nonlinear dynamic analysis is a widely adopted computational methodology to ensure a realistic seismic assessment that accounts for the structure's nonlinearity [5]. A complex structural simulation was carried out using the finite element-based Abaqus on a high-performance computing system equipped with a NVIDIA GeForce RTX 3060 and 64GB RAM. Due to the rectangular plan configuration, the vulnerability assessment was performed in both principal directions. Seven central nodes are assigned floor-wise to evaluate the dynamic responses in terms of displacement, drift, and acceleration. The outcome contributes to a deeper understanding of the structural vulnerabilities of the Bhairabnath temple under varying seismic excitations.

5.1 Dynamic responses of the structure

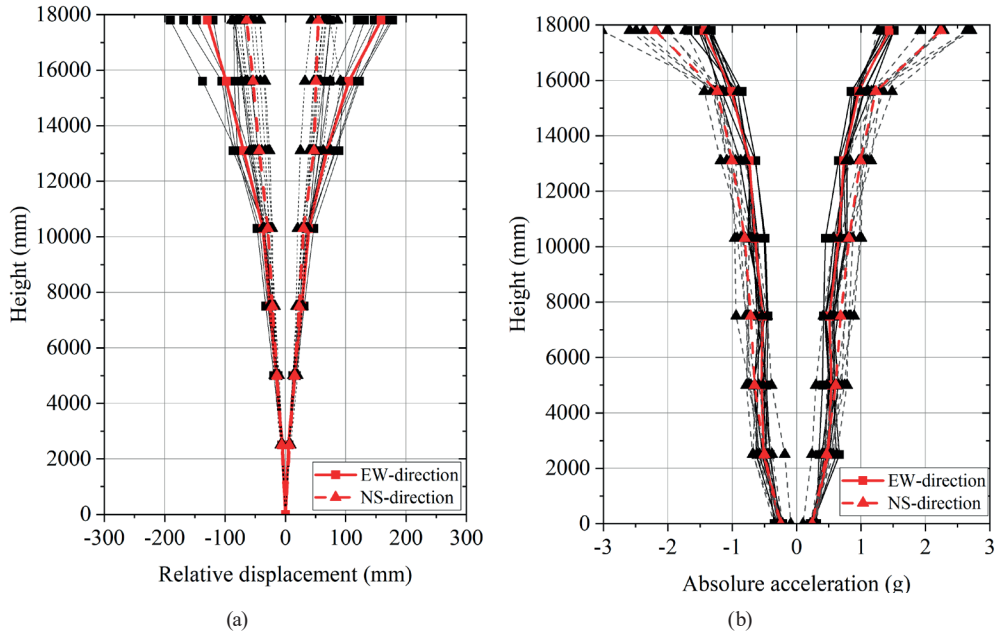
The structure's nonlinear dynamic response exhibits pronounced directionality dependency, as presented in Table 6. Similarly, the floor-wise responses are illustrated in Fig. 8, which shows a nonuniform distribution of responses caused by the vertical irregularities.

5.1.1 Horizontal displacement

The peak relative roof displacements in the EW direction are larger than in the NS direction, indicating a flexible response in the EW direction. In the EW direction, the average peak relative displacement reaches 158.38 mm, and is constrained in the NS direction with an average value of 69.04 mm. This discrepancy is primarily governed by the rectangular base configuration and setback configuration at each section along the vertical direction that consecutively reduces the exterior dimension and wall thickness at

Table 6 Individual dynamic response of the historical pagoda structure

Earthquake	Maximum relative displacement (mm)		Maximum top absolute acceleration (g)		Maximum base shear (kN)	
	EW-direction	NS-direction	EW-direction	NS-direction	EW-direction	NS-direction
Coyote_150	131.33	68.13	1.47	2.23	2822.41	3792.11
Irpnia_285	147.25	75.32	1.51	2.64	2625.05	3453.79
MorganHill_459	174.57	86.31	1.41	2.01	2448.69	3487.30
Northridge_1013	119.28	54.52	1.51	2.06	2616.87	3024.95
Koceli_1161	177.54	62.08	1.49	2.29	2403.25	3878.65
Koceli_1165	149.88	73.4	1.33	2.66	2595.08	4032.65
ChiChi_1511	168.46	80.58	1.51	2.21	2521.37	3795.27
LaqAila_4483	166.25	54.59	1.39	2.23	2688.19	4004.20
Duazce_8164	190.86	66.47	1.33	2.71	2486.07	3515.55
Average	158.38	69.04	1.44	2.34	2822.41	3664.94
Minimum	131.33	54.52	1.33	2.01	2822.41	3024.95
Maximum	190.86	86.31	1.51	2.71	2822.41	4032.65



(a) (b)

Fig. 8 Floor-wise dynamic response of the structure, (a) relative displacement vs height, (b) absolute acceleration vs height of the structure

the upper floor, which results in a higher flexibility along the shorter dimension. The graphical plots of floor-wise displacement response are illustrated in Fig. 8(a).

Due to the setback configuration of the masonry pagoda structure, the upper section typically has thinner walls, more openings, and lighter structural framing. This consequently reduces significant mass and stiffness in the upper sections.

Despite the reduction in floor mass toward the upper tiers, the observed displacement amplification indicates that the vertical stiffness irregularity arising from the progressive tapering of wall thickness tends to dominate the dynamic response over the mitigating effect of reduced mass. As shown in Fig 8(a), the variation of the deformation in height for the fixed base structure is consistent and has linear growth up to the fourth floor in the EW direction. Meanwhile, the large opening and unconnected middle wall section to the exterior wall experience higher nonlinear behavior at the fifth floor and eventually extend above.

5.1.2 Horizontal acceleration

Similarly, the absolute floor-wise acceleration is illustrated in Fig. 8(b). The higher acceleration demand on the top floor indicates significant dynamic amplification leading to higher inertial forces despite the relatively lower floor mass of the top floor compared to the bottom section.

In the EW direction, the top acceleration is amplified up to three times, and six times in the NS direction. The excessive amplification at the top is due to the whip effects, which occurred mostly in the vertical irregularities and disproportionate mass distribution of the pagoda structure. The whip effects on the dynamic performance of the pagoda structure studied by Wu et al. [46] observed the acceleration amplification at the top of the pagoda structure to be nine times and the displacement amplification to be eight to ten times.

The directional disparity between displacement and acceleration demand indicates larger relative displacement but lower spectral acceleration in the EW direction, and the reverse in the NS direction, as presented in Table 6. The EW direction exhibits greater period elongation due to more pronounced stiffness loss, shifting its response into the displacement-sensitive region of the near-fault spectra, while the NS direction retains stiffness closer to its elastic state, keeping its response in acceleration-sensitive regions. This directional asymmetry likely reflects underlying plan irregularity in wall thickness and opening distribution between the two orthogonal axes of the pagoda structure.

5.1.3 Inter-storey drift

As the structure exceeds the linear state, the EW direction profiles exhibit significant dispersion, particularly at the upper floor levels. The plot highlights the sensitivity of the low-strength masonry structure to the characteristics of the ground motion. Moreover, for an unreinforced masonry structure characterized by low tensile strength and brittle failure modes, displacement alone is not a sufficient performance index. The inter-storey drift ratio, which correlates more directly with localized masonry cracking and shear failure, must be evaluated to quantify the true degree of vulnerability.

Unlike the displacement response, the inter-storey drift highlights the concentration of seismic demand at specific floors as presented in Fig. 9. In the EW direction, the seismic demand is notably severe, with peak drifts consecutively occurring at the upper floors. The three limit states for unreinforced historical masonry structures are classified as Limited Damage level (LD), Controlled Damage level (CD), and Collapse Prevention level (CP) with critical limit values of H/333 (0.3%), H/142 (0.7%), and H/100 (1%), respectively [47]. In Fig. 9, the blue line represents the limit state considered in the study. It represents the suite of earthquakes that exhibits a high degree of dispersion, with

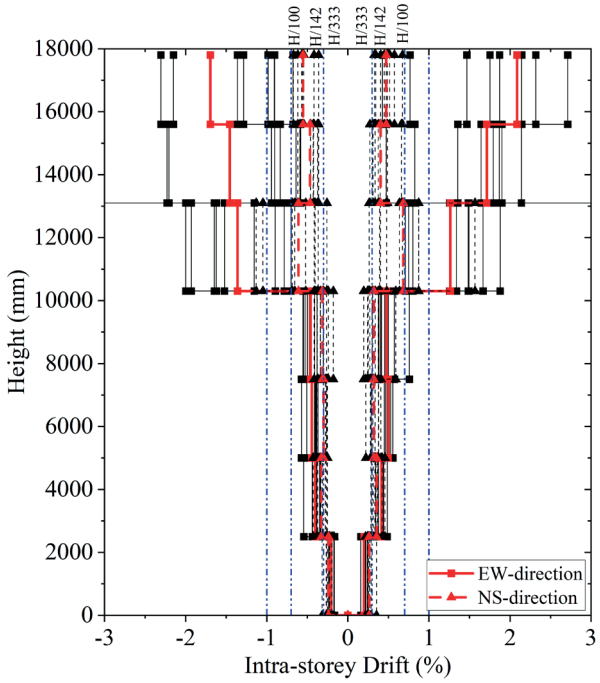


Fig. 9 Floor wise response of the structure in terms of Inter-storey drift

several individual records exceeding the CP drift threshold at the top floor in the EW direction. On the other hand, the NS direction maintains a much stiffer response, with most records remaining within the CD drift limit.

The bulging of the drift response at the fifth floor in both directions identifies a critical region of stiffness discontinuity due to the wide openings in the structure. Above the fifth floor, the drift limit exceeds the CP limit in the EW direction, however, the NS direction drift remains within the CD limit. Moreover, the lower section of the structure remains within the CD range. The localization of deformation indicates that the inter-storey drift response is crucial for pinpointing the precise weakness in the masonry structure, even while displacement presents a wide view of structural flexibility.

Comparing the dynamic responses of the structure, the structure is relatively stable at the bottom section, whereas it is highly vulnerable in the middle and top sections. This is due to the whip effects in the pagoda structure caused when the relative mass and stiffness in the structure are irregular throughout the vertical direction.

5.1.4 Stiffness degradation and hysteresis energy dissipation

The nonlinear time-history response of the pagoda structure is presented in terms of base shear versus peak relative displacement hysteresis loops, as illustrated in Fig. 10. Stiffness degradation and hysteretic energy dissipation,

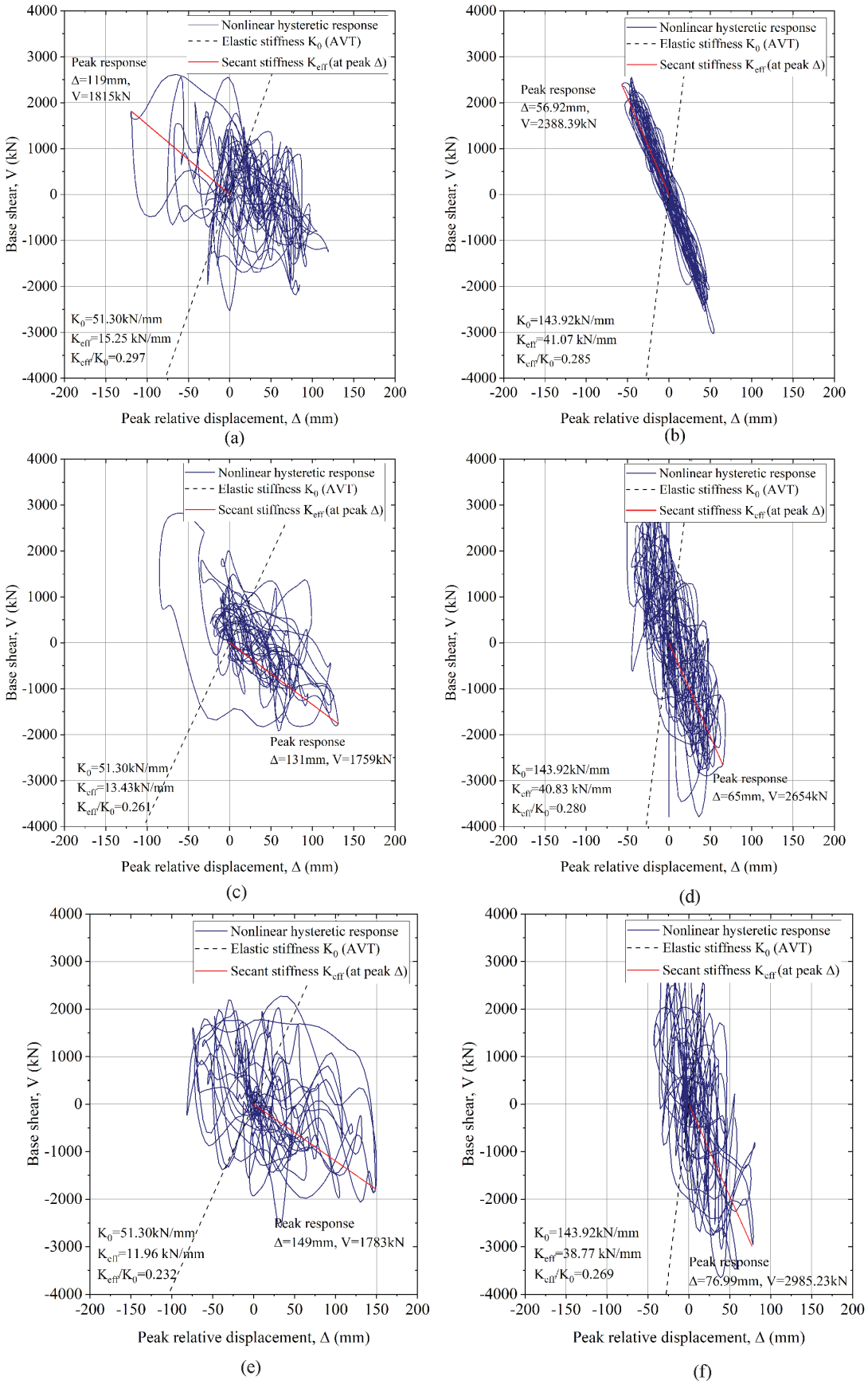


Fig. 10 Base shear vs peak relative displacement of three representative earthquake in EW- and NS-direction, (a)-(b) Northridge earthquake, (c-d) Coyote earthquake, and (e-f) Koceli earthquake

considered as two structural performance measures, were derived. Stiffness degradation is quantified through the ratio of secant-to-elastic stiffness (K_{eff}/K_0), and hysteretic energy dissipation is quantified through the area enclosed by each loop.

The initial elastic stiffness (K_0) was obtained from the AVT-calibrated FE model and represents the theoretical linear-elastic backbone response, from Table 4, prior to the onset of masonry cracking, shown as the dashed reference line in each subplot. The secant stiffness at peak response, K_{eff}, was computed as the slope of the line connecting the origin to the peak coordinate for each ground motion record and is superimposed on the corresponding loop (red line). Throughout the input ground motions, K_{eff}/K_0 ranged from 0.221 to 0.297 in the EW-direction and from 0.257 to 0.345 in the NS- direction, indicating that the structure retained only 22 to 29% of its initial elastic stiffness at peak demand in the EW-direction, compared to 25 to 34% in the NS- direction. The effective-to-initial stiffness in both directions is presented in Table 7. This directional disparity is consistently observed across the suite of independent ground motion records. The obtained behavior is interpreted as a structural characteristic rather than a record-dependent artifact, and is attributed to unequal masonry wall thickness and opening distribution between the two orthogonal axes of the pagoda plan.

The shape of the hysteresis loops provides additional physical insight beyond the secant stiffness ratio alone. In the EW-direction, the loops exhibit a wide, irregular envelope dominated by a single large excursion corresponding to the governing near-fault velocity pulse, superimposed with numerous smaller, pinched loops clustered near the origin during excitations. The pronounced pinching, a marked reduction in loop width, and consequently in tangent stiffness, as the response passes through zero force, is characteristic of the cracks in the masonry wall piers during excitation, and reflects a loss of stiffness degradation. In contrast, the NS-direction loops are narrow and spindle-shaped, remaining close to the elastic stiffness line throughout the response history, with limited separation between loading and unloading branches, consistent with a predominantly elastic response and comparatively minor masonry damage.

The area enclosed by a force–displacement loop corresponds to the hysteretic energy dissipated by the structure. The qualitative difference in loop geometry between the two directions corresponds to a substantial difference in cumulative energy dissipation. The wide, pinched loops in the EW direction, despite lower peak base shear than the NS direction, enclose a visibly larger cumulative area and therefore dissipate more hysteretic energy, consistent with their lower K_{eff}/K_0 ratio. This indicates that the EW-direction accommodated seismic demand primarily through inelastic damage mechanisms, through wall cracking, whereas the NS-direction walls resisted demand largely within their elastic capacity, attracting higher force but undergoing comparatively limited damage. Cumulative hysteretic energy dissipation for each record and corresponding direction is reported in Table 7, which represents the irrecoverable energy dissipated through inelastic material response.

Collectively, these results demonstrate that stiffness degradation (K_{eff}/K_0) and hysteretic energy dissipation are complementary, physically consistent indicators of

Table 7 Stiffness reduction and hysteretic energy dissipation of the structure

Earthquake	K_{eff}/K_0		Cumulative hysteretic energy dissipation (kJ)	
	EW	NS	EW	NS
Coyote_150	0.261	0.282	62.48	50.02
Irpnia_285	0.225	0.266	213.68	54.59
MorganHill_459	0.221	0.276	146.71	73.02
Northridge_1013	0.297	0.285	89.07	17.56
Koceli_1161	0.247	0.345	138.78	86.23
Koceli_1165	0.232	0.269	138.59	80.09
ChiChi_1511	0.237	0.292	115.95	70.25
LaqAila_4483	0.230	0.257	154.74	87.64
Duazce_8164	0.263	0.299	131.16	30.99
Average	0.246	0.286	132.35	68.194
Minimum	0.221	0.257	62.48	17.56
Maximum	0.297	0.345	213.68	87.64

directional damage asymmetry in the pagoda structure, with the EW direction exhibiting behavior indicative of significant masonry damage and the NS direction retaining near-elastic performance under the same suite of near-fault ground motions.

5.5.5 Damage detection

Figs. 11 and 12 illustrate the progression of compressive and tensile damage in the Bhairabnath temple under the Northridge and Morgan Hill earthquakes. This damage pattern was concentrated at the upper tiers, fifth-floor openings, and base corners, and was consistent with the interstory drift and stiffness degradation trends observed across the full nine-record suite.

The damage distribution reveals two distinct mechanisms operating at markedly different severities. Considering the low shear strength of masonry structures, tensile damage is more significant than compression damage. The tensile damage initiates more rapidly and propagates more extensively, as shown in Figs. 11 and 12. Tensile damage (DAMAGET), reaching a peak value of 0.948, indicates near-complete degradation of tensile stiffness at the most affected locations and reflects progressive cracking under excitations. Tensile damage is the dominant failure mechanism in this structure. Compression damage (DAMAGEC), reaching only 0.326, remains secondary and spatially confined to the base-story corners, consistent with localized crushing under the compressive component of the overturning moment. This pattern of damage lines up with what the drift and stiffness results already suggested. Due to the setback configuration, the upper section reduces its exterior dimensions and wall thickness, generating a whipping effect through the height of the structure. The fifth-floor wide openings act as geometric stress concentrators, redistributing load around the corners of an opening, and initiate cracking, as illustrated in Fig. 11 and 12.

The substantially greater extent and intensity of tensile damage in the EW direction relative to NS is consistent with its lower fundamental frequency and larger displacement demand. As a result, it activates and propagates a greater number of tensile crack surfaces throughout the structure. Furthermore, directional vulnerability was compared between the principal directions. For the input motions, the structure exhibits greater susceptibility to damage in the EW direction. The outcomes are attributed to the stiffness variation and low shear strength inherent to the masonry structure.

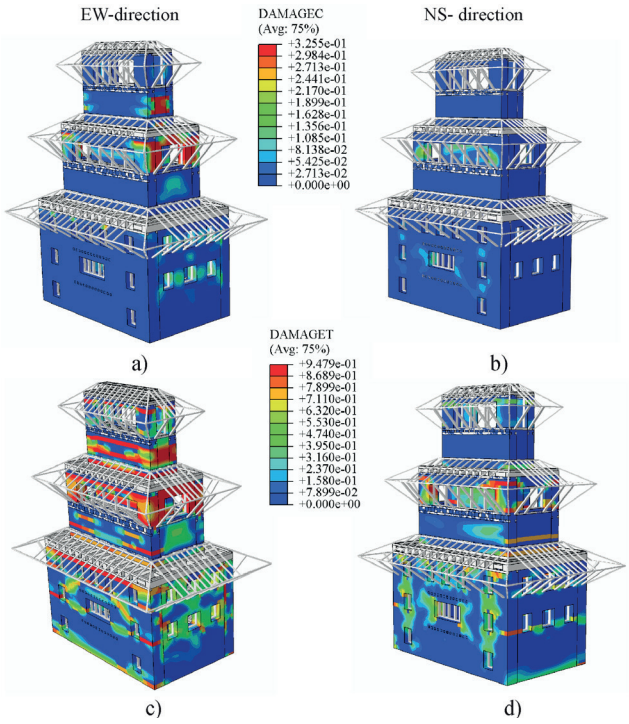


Fig. 11 Structural damage under nonlinear time history analysis under Northridge earthquake (a,b) compression damage in the EW- and NS-direction respectively (DAMAGEC) , (c,d) tensile damage in EW- and NS- direction (DAMAGET)

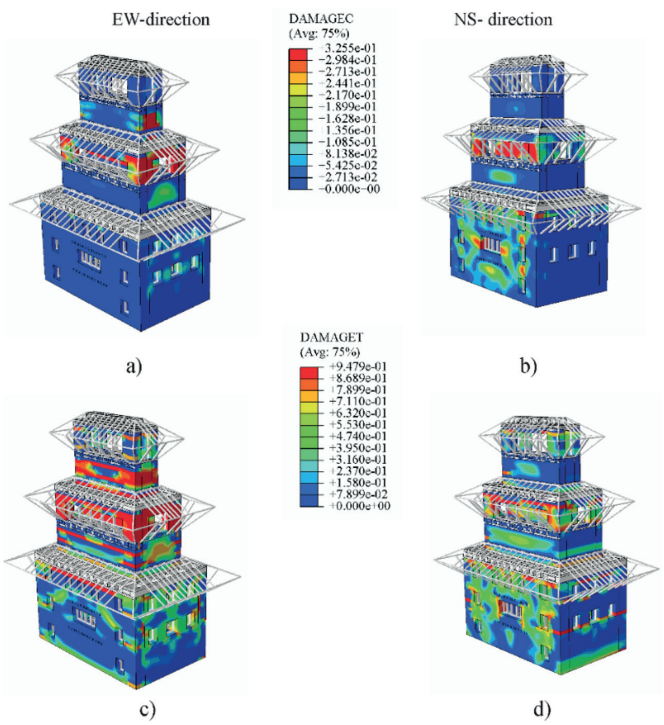


Fig. 12 Structural damage under nonlinear time history analysis under MorganHill earthquake (a,b) compression damage in the EW- and NS-direction respectively (DAMAGEC) , (c,d) tensile damage in EW- and NS- direction (DAMAGET)

6 Conclusions

The study presents a comprehensive seismic performance evaluation of the multi-tiered Bhairabnath temple carried out through an experimentally conducted ambient vibration test combined with nonlinear dynamic analysis under near-fault earthquakes. The developed finite element model was calibrated against the AVT results to assess the reliability of the results. The study highlights the vulnerability of historical structures in terms of displacement, acceleration, inter-storey drift, and damage state. Hence, the findings yield essential insights for recommending appropriate strengthening techniques to preserve and conserve the historical structures. The following conclusions were generated from the nonlinear dynamic analysis of the Bhairabnath temple:

1. Ambient vibration testing identified the fundamental natural frequencies of the pagoda structure as 1.59 Hz in the EW direction and 2.50 Hz in the NS direction, revealing an inherent directional asymmetry in the structure's dynamic behavior, and the FE model was subsequently calibrated through iterative model updating against these AVT-measured frequencies.
2. The masonry pagoda structure exhibits a highly direction-dependent dynamic response. The stiffer NS direction generates higher acceleration and base shear at the expense of smaller displacement. Conversely, the relatively flexible EW direction produces a larger displacement under lower force demand.
3. The EW- direction exhibited wide, pinched hysteresis loops characteristic of earthquake excitations, dissipating more cumulative hysteretic energy than the stiffer, near-elastic NS direction, despite carrying a lower peak base shear demand.
4. CDP results confirmed tensile cracking as the dominant failure mechanism, with compressive damage remaining secondary. Damage concentrated at the tapering upper section owing to disproportionate stiffness and mass, at the fifth-floor openings due to geometric stress concentration, and at the base corners due to cumulative overturning effects, consistent with the observed stiffness degradation trends.
5. The consistency across modal properties, hysteretic response, and damage indices shows that directional stiffness irregularity, rather than ground motion variability alone, governs the seismic vulnerability of pagoda-style masonry temples, highlighting the need for direction-specific retrofit strategies targeting the weaker direction.

Future studies could extend the present framework by incorporating experimental validation, probabilistic seismic assessment approaches, and the influence of structural irregularities, further enhancing the reliability and generalizability of seismic vulnerability predictions for historical masonry structures.

Acknowledgement

The authors sincerely express gratitude to the Bhaktapur Municipality and Khwopa College of Engineering for granting us the necessary permission to conduct the test within the historical structure, which was instrumental in completing this research. The authors truly appreciate Dr. Subegman Bijukchhen, Khwopa Engineering College, for their invaluable guidance and contribution in conducting the experimental test.

Declaration of conflicting interests

The author(s) declared no potential conflicts of interest concerning this article's research, authorship, and/or publication.

Funding

This work was financially supported by the State Key Laboratory of Disaster Reduction in Civil Engineering (Grant No. SLDRCE19-B-29).

References

[1] Saisi, A., Borlenghi, P., Gentile, C. "Non-Destructive Testing and Synergistic Investigation of a Historic Tower", Buildings, 14(4), 1101, 2024. https://doi.org/10.3390/buildings14041101

[2] Asteris, P. G., Douvika, M. G., Apostolopoulou, M., Moropoulou, A. "Seismic and Restoration Assessment of Monumental Masonry Structures", Materials, 10(8), 895, 2017. https://doi.org/10.3390/ma10080895

[3] Puncello, I., Caprili, S. "Seismic Assessment of Historical Masonry Buildings at Different Scale Levels: A Review", Applied Sciences, 13(3), 1941, 2023. https://doi.org/10.3390/app13031941

[4] Roca, P., Cervera, M., Gariup, G., Pela', L. "Structural Analysis of Masonry Historical Constructions. Classical and Advanced Approaches", Archives of Computational Methods in Engineering, 17(3), pp. 299-325, 2010. https://doi.org/10.1007/s11831-010-9046-1

[5] Altunişik, A. C., Günaydin, M., Ertürk Atmaca, E., Genç, A. F., Okur, F. Y., Sevim, B. "Experimental measurement-based FE model updating and seismic response of Santa Maria Church and its guest-house building", Journal of Civil Structural Health Monitoring, 14(3), pp. 663-692, 2024. https://doi.org/10.1007/s13349-023-00747-9

[6] Cannizzaro, F., Castellazzi, G., Grillanda, N., Pantò, B., M. Petracca, M. "Modelling the nonlinear static response of a 2-storey URM benchmark case study: comparison among different modelling strategies using two- and three-dimensional elements", Bulletin of Earthquake Engineering, 20(4), pp. 2085-2114, 2022. https://doi.org/10.1007/s10518-021-01183-0

[7] Standoli, G., Giordano, E., Milani, G., Clementi, F. "Model Updating of Historical Belfries Based on Oma Identification Techniques", International Journal of Architectural Heritage, 15(1), pp. 132-156, 2021. https://doi.org/10.1080/15583058.2020.1723735

[8] Soltani, Y., Sadhu, A. "Non-destructive techniques for masonry structures: from geometry extraction to damage identification", Engineering Research Express, 8(10), 2026. https://doi.org/10.1088/2631-8695/ae696e

[9] Alqurashi, I., Alver, N., Bagci, U., Catbas, F. N. "A Review of Ultrasonic Testing and Evaluation Methods with Applications in Civil NDT/E", Journal of Nondestructive Evaluation, 44(2), 53, 2025. https://doi.org/10.1007/s10921-025-01190-0

[10] Demir, A., Nohutcu, H., Ercan, E., Hokelekli, E., Altintas, G. "Effect of model calibration on seismic behaviour of a historical mosque", Structural Engineering and Mechanics, 60(5), pp. 749-760, 2016. https://doi.org/10.12989/sem.2016.60.5.749

[11] Song, X., Wu, Y., Li, K., Jin, L., Chen, F., Liu, X., Dou, X. "Mechanical behaviour of Chinese traditional timber pagoda during Construction", Engineering Structures, 196, 109302, 2019. https://doi.org/10.1016/j.engstruct.2019.109302

[12] Sudarsana, I. K., Susila, G. A., Silvi, N. P., Dwijendra, N. K. A. "Seismic Analysis on the Behaviors of Meru Structures: A Sacred Building in Balinese Temples", Modelling and Simulation in Engineering, 2022(1), 1846193, 2022. https://doi.org/10.1155/2022/1846193

[13] Günaydin, M. "Seismic performance evaluation of a fire-exposed historical structure using an updated finite element model" Engineering Failure Analysis, 106, 104149, 2019. https://doi.org/10.1016/j.engfailanal.2019.104149

[14] Lu, J., Tian, J., Wang, Z., Jiang, F., Wu, X. "Analysis of seismic damage and seismic capacity of the structure of the ultrahigh pagoda", The Structural Design of Tall and Special Buildings, 33(17), 2024. https://doi.org/10.1002/tal.2181

[15] Jaishi, B., Ren, W.-X., Zong, Z.-H., Maskey, P. N. "Dynamic and seismic performance of old multi-tiered temples in Nepal", Engineering Structures, 25(14), pp. 1827-1839, 2003. https://doi.org/10.1016/j.engstruct.2003.08.006

[16] Fujita, K., Ponce, D., Toyoda, T., Morii, M., Niitsu, Y., Hanazato, T., Subedi, J., Shakya, M. "Microtremor Measurement and Damage Investigation of Historical Timber–masonry Composite Tiered Temples in Nepal", International Journal of Architectural Heritage, 16(4), pp. 518-537, 2022. https://doi.org/10.1080/15583058.2020.1808909

[17] Gentile, C., Saisi, A. "Ambient vibration testing of historic masonry towers for structural identification and damage assessment", Construction and Building Materials, 21(6), pp. 1311-1321, 2007. https://doi.org/10.1016/j.conbuildmat.2006.01.007

[18] Xu, D., Xie, Q., Hao, W. "Seismic damage evaluation of historical masonry towers through numerical model", Bulletin of Earthquake Engineering, 22(4), pp. 2235-2266, 2024. https://doi.org/10.1007/s10518-024-01858-4

[19] Pejatovic, M., Sarhosis, V., Milani, G. "Multi-tiered Nepalese temples: Advanced numerical investigations for assessing performance at failure under horizontal loads", Engineering Failure Analysis, 106, 104172, 2019. https://doi.org/10.1016/j.engfailanal.2019.104172

[20] Dais, D., Sarhosis, V., Smyrou, E., Bal, İ. E. "Seismic intervention options for multi-tiered Nepalese Pagodas: The case study of Jaisedewal temple", Engineering Failure Analysis, 123, 2021. https://doi.org/10.1016/j.engfailanal.2021.105262

[21] Saygılı, Ö., Lemos, J. V., Moghimi, S. "Site Specific Hazard Assessment and Multi-Level Seismic Performance Evaluation of Historical Mosque", International Journal of Architectural Heritage, 18(7), pp. 1143-1163, 2024. https://doi.org/10.1080/15583058.2023.2216175

[22] Shilpakar, R., Maskey, P. N., Silpakar, P. "Construction technology of multi-tiered temples and their rehabilitation after 2015 April Earthquake in Bhaktapur", Progress in Disaster Science, 10, 100177, 2021. https://doi.org/10.1016/j.pdisas.2021.100177

[23] Romero-Sánchez, E., Morales-Esteban, A., Bento, R., Navarro-Casas, J. "Numerical modelling for the seismic assessment of complex masonry heritage buildings: the case study of the Giralda tower", Bulletin of Earthquake Engineering, 21(9), pp. 4669-4701, 2023. https://doi.org/10.1007/s10518-023-01714-x

[24] Dassault Systèmes SIMULIA Corp., "Abaqus Documentation" [online]. Available at: http://130.149.89.49:2080/v2016/index.html (Accessed 15 May 2026)

[25] Gonçalves, M., Ponte, M., Bento, R. "Seismic Assessment of Existing Masonry Buildings Using Damage Mechanics", Buildings, 14(8), 2395, 2024. https://doi.org/10.3390/buildings14082395

[26] D'Altri, A. M., Sarhosis, V., Milani, G., Rots, J., Cattari, S., Lagomarsino, S., Sacco, E., Tralli, A., Castellazzi, G., de Miranda, S. "Modeling Strategies for the Computational Analysis of Unreinforced Masonry Structures: Review and Classification", Archives of Computational Methods in Engineering, 27(4), pp. 1153–1185, 2020. https://doi.org/10.1007/s11831-019-09351-x

[27] Singhal, V., Rai, D. C. "Role of Toothing on In-Plane and Out-of-Plane Behavior of Confined Masonry Walls", Journal of Structural Engineering, 140(9), 04014053, 2014. https://doi.org/10.1061/(ASCE)ST.1943-541X.0000947

[28] Cattari, S., Calderoni, B., Caliò, I., Camata, G., de Miranda, S., Magenes, G., Milani, G., Saetta, A. "Nonlinear modeling of the seismic response of masonry structures: critical review and open issues towards engineering practice", Bulletin of Earthquake Engineering, 20(4), pp. 1939-1997, 2022. https://doi.org/10.1007/s10518-021-01263-1

[29] D'Altri, A. M., Cannizzaro, F., Petracca, M., Talledo, D. A. "Nonlinear modelling of the seismic response of masonry structures: Calibration strategies", Bulletin of Earthquake Engineering, 20(4), pp. 1999-2043, 2022.
https://doi.org/10.1007/s10518-021-01104-1

[30] Endo, Y., Miyoshi, K. "Meso-scale numerical simulation of the mechanical behaviour of brick masonry in earth mortar", Journal of Building Engineering, 74, 106890, 2023.
https://10.1016/j.jobe.2023.106890

[31] Soti, R., Abdulrahman, L., Barbosa, A. R., Wood, R. L., Mohammadi, M. E., Olsen, M. J. "Case study: Post-earthquake model updating of a heritage pagoda masonry temple using AEM and FEM", Engineering Structures, 206, 109950, 2020.
https://doi.org/10.1016/j.engstruct.2019.109950

[32] Endo, Y., Hanazato, T. "Seismic Analysis of a Three-Tiered Pagoda Temple Affected by the 2015 Gorkha Earthquake", International Journal of Architectural Heritage, 14(3), pp. 457-470, 2020.
https://doi.org/10.1080/15583058.2018.1550534

[33] Spoldi, E., Russo, S. "Damage Assessment and Dynamic Characteristics of Temples in Nepal Post Gorkha 2015 Earthquake", International Journal of Architectural Heritage, 15(3), pp. 479-493, 2021.
https://doi.org/10.1080/15583058.2019.1628322

[34] Castellazzi, G., D'Altri, A. M., de Miranda, S., Ubertini, F. "An innovative numerical modeling strategy for the structural analysis of historical monumental buildings", Engineering Structures, 132, pp. 229-248, 2017.
https://doi.org/10.1016/j.engstruct.2016.11.032

[35] Lubliner, Oliver, J., Oller, S., Oñate, E. "A plastic-damage model for concrete", International Journal of Solids and Structures, 25(3), pp. 299-326, 1989.
https://doi.org/10.1016/0020-7683(89)90050-4

[36] Lee, J., Fenves, G. L. "Plastic-Damage Model for Cyclic Loading of Concrete Structures", Journal of Engineering Mechanics, 124(8), pp. 892-900, 1998.
https://10.1061/(ASCE)0733-9399(1998)124:8(892)

[37] Rainone, L. S., Tateo, V., Casolo, S., Uva, G. "About the Use of Concrete Damage Plasticity for Modeling Masonry Post-Elastic Behavior", Buildings, 13(8), 1915, 2023.
https://doi.org/10.3390/buildings13081915

[38] Bray, J. D., Rodriguez-Marek, A. "Characterization of forward-directivity ground motions in the near-fault region", Soil Dynamics and Earthquake Engineering, 24(11), pp. 815-828, 2004.
https://doi.org/10.1016/j.soildyn.2004.05.001

[39] Wang, G., Youngs, R., Power, M., Li, Z. "Design Ground Motion Library: An Interactive Tool for Selecting Earthquake Ground Motions", Earthquake Spectra, 31(2), pp. 617-635, 2015.
https://doi.org/10.1193/090612eqs283m

[40] Sadeghi Movahhed, A., Shirkhani, A., Zardari, S., Noroozinejad Farsangi, E., Karimi Pour, A. "Effective range of base isolation design parameters to improve structural performance under far and near-fault earthquakes," Advances in Structural Engineering, 26(1), pp. 52-71, 2023.
https://doi.org/10.1177/13694332221119870

[41] Bilgin, H. "Effects of near-fault and far-fault ground motions on nonlinear dynamic response and seismic damage of masonry structures" Engineering Structures, 300, 117200, 2024.
https://doi.org/10.1016/j.engstruct.2023.117200

[42] Pacific Earthquake Engineering Research Center (PEER) "NGA-West2 Database" [online] Available at: https://ngawest2.berkeley.edu/ (Accessed 15 May 2026)

[43] American Society of Civil Engineers "Minimum Design Loads for Buildings and Other Structures", American Society of Civil Engineers, Reston, VA, USA, ASCE/SEI 7-10, 2010.

[44] Prajapati, A., Zhao, B. "Investigating the Site Response Variability of Deep Sedimentary Column Induced by Varying Soil Friction Angles", Periodica Polytechnica Civil Engineering, 69(1), pp. 308-320, 2025.
https://doi.org/10.3311/PPci.37882

[45] Al Atik, L., Abrahamson, N. "An Improved Method for Nonstationary Spectral Matching", Earthquake Spectra, 26(3), pp. 601-617, 2010.
https://doi.org/10.1193/1.3459159

[46] Wu, X., Lu, J., Wang, Z., Yang, W., Qiao, N. "Dynamic characteristics and seismic response analysis of the bottle-shaped masonry ancient pagoda", Structures, 44, pp. 1648-1659, 2022.
https://doi.org/10.1016/j.istruc.2022.08.109

[47] Ahunbay, Z., Altay, G., Arun, E. G., Aydemir, O., Atasagun, F. D. et al. "A Guideline for Earthquake Risk Management of Historical Structures in Turkey", In: 4th International Conference on Earthquake Engineering and Seismology, Eskişehir, Turkey, 2017.